ACS APPLIED MATERIALS & INTERFACES

www.acsami.org Research Article

Structural and Elastic Properties of Empty-Pore Metalattices Extracted *via* Nondestructive Coherent Extreme UV Scatterometry and Electron Tomography

Joshua L. Knobloch,* Brendan McBennett, Charles S. Bevis, Sadegh Yazdi, Travis D. Frazer, Amitava Adak, Emma E. Nelson, Jorge N. Hernández-Charpak, Hiu Y. Cheng, Alex J. Grede, Pratibha Mahale, Nabila Nabi Nova, Noel C. Giebink, Thomas E. Mallouk, John V. Badding, Henry C. Kapteyn, Begoña Abad, and Margaret M. Murnane

Cite This: *ACS Appl. Mater. Interfaces* 2022, 14, 41316−41327 Read Online

ABSTRACT: Semiconductor metalattices consisting of a linked network of three-dimensional nanostructures with periodicities on a length scale <100 nm can enable tailored functional properties due to their complex nanostructuring. For example, by controlling both the porosity and pore size, thermal transport in these phononic metalattices can be tuned, making them promising candidates for efficient thermoelectrics or thermal rectifiers. Thus, the ability to characterize the porosity, and other physical properties, of metalattices is critical but challenging, due to their nanoscale structure and thickness. To date, only metalattices with high porosities, close to the close-packing fraction of hard spheres, have been studied experimentally. Here, we characterize the porosity, thickness, and elastic properties of a low-porosity, empty-pore silicon metalattice film (∼500 nm thickness) with periodic spherical pores (∼tens of nanometers), for the first time. We use laser-driven nanoscale surface acoustic waves probed by extreme ultraviolet scatterometry to nondestructively measure the acoustic dispersion in these thin silicon metalattice layers. By comparing the data to finite element models of the metalattice sample, we can extract Young's modulus and porosity. Moreover, by controlling the acoustic wave penetration depth, we can also determine the metalattice layer thickness and verify the substrate properties. Additionally, we utilize electron tomography images of the metalattice to verify the geometry and validate the porosity extracted from scatterometry. These advanced characterization techniques are critical for informed and iterative fabrication of energy-efficient devices based on nanostructured metamaterials.

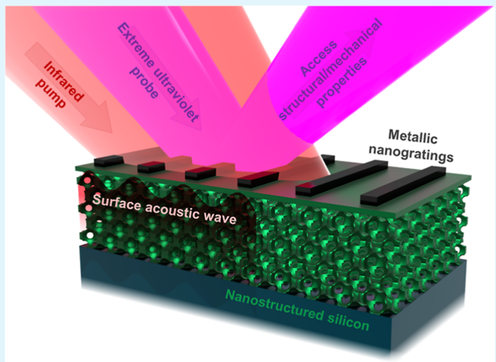

KEYWORDS: *metalattice, porosity, mechanical properties, high harmonics, laser, acoustic metrology*

INTRODUCTION

Nanostructured materials can exhibit exotic properties and behaviors that enrich the landscape of bulk materials, due to the increased influence of surfaces,[1−3] geometry,[4−6] and interfaces.[7] The novel physics that governs these systems arises because the nanoscale features are on the same characteristic length scales as the fundamental energy carriers, such as phonons, electrons, and magnons. In particular, phononic crystals—periodic structures with a specific symmetry embedded in an elastic medium—represent a promising route for engineering sound and heat flow for a variety of applications.[8,9] By manipulating the phonon behavior using periodic scattering features, recent studies have demonstrated that phononic crystals can advance efficient thermoelectric devices,[10] interfacial transport materials,[11] thermal diodes and rectifiers,[12] ultralight high-strength materials,[13] and even "phonon lasers".[14] Thus, experimentally accessing and theoretically predicting the behaviors and properties of nanoscale phononic crystals is critical for incorporating them into new technologies yet challenging due to their feature sizes on the order of tens of nanometers.

Metalattices are a type of 3D phononic crystal consisting of periodic nanospheres embedded in a host medium. With periodicity well below 100 nm, metalattices contain single-nanometer-scale feature sizes, distinguishing them from inverse opals, which are analogous materials on much larger scales. Due to their deep nanoscale features, they exhibit unique material behaviors; for example, metallic metalattices possess

Received: June 1, 2022
Accepted: August 2, 2022
Published: September 2, 2022

https://doi.org/10.1021/acsami.2c09360
ACS Appl. Mater. Interfaces 2022, 14, 41316−41327

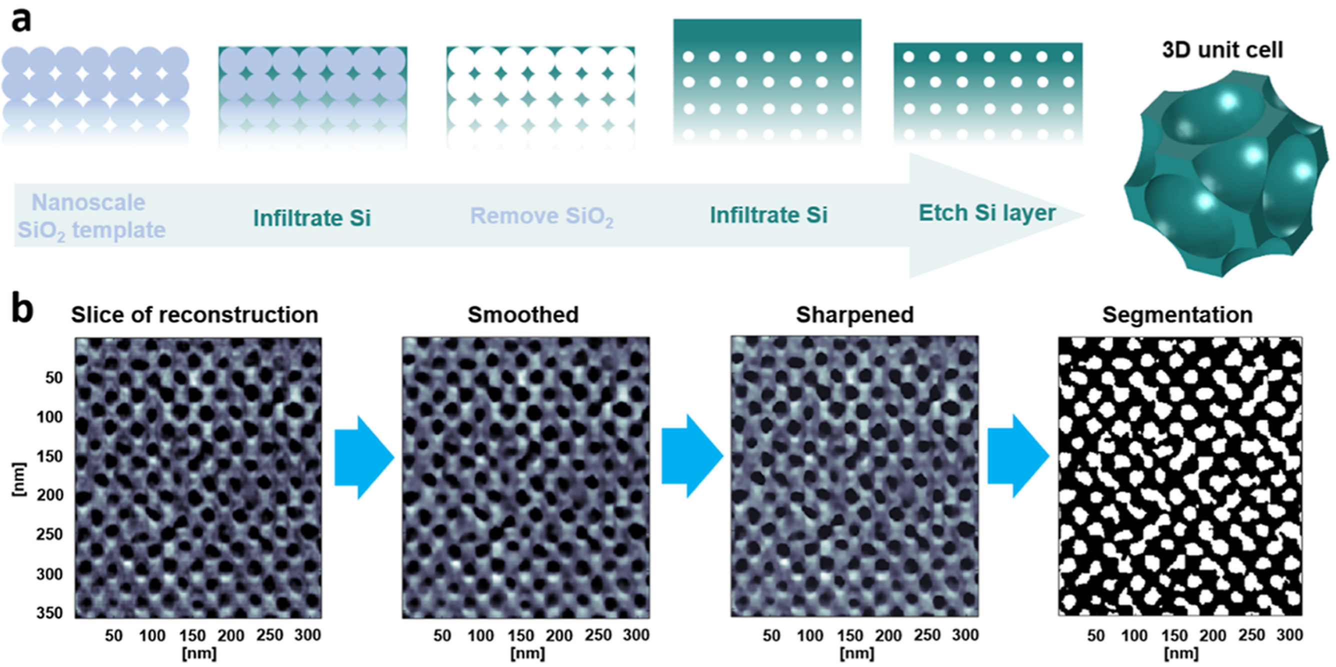

Figure 1. (a) Fabrication of the silicon metalattices. We assemble colloidal solutions of ∼30 nm silica nanospheres into a close packed template film on a silicon substrate. Silicon is infiltrated into the interstitial regions of the template using high-pressure confined chemical vapor deposition. The silica nanospheres are then etched away with hydrofluoric acid vapor. The porosity was reduced below the limit of close-packing spheres by infiltrating silicon a second time. We anneal the sample to crystallize the infiltrated amorphous silicon and utilize reactive ion etching to remove the silicon overlayer after each infiltration. An idealized model of the high-porosity metalattice unit cell is shown. (b) Porosity characterization from scanning transmission electron microscopy. To remove noise, the tomography data set is sliced into 2D images which are smoothed and sharpened by the anisotropic diffusion and unsharp mask sharpening filters, respectively. The 3D tomography image is then segmented using three different algorithms: global and local thresholding and *k*-means clustering. In the resulting image, the black pixels correspond to silicon and the white to void.

multiple topological magnetic phases,[2,3,15,16] while semiconductor metalattices display tunable thermal and mechanical properties. Nanostructured metalattices are created by first assembling silica nanospheres into colloidal crystal thin films and then infiltrating the interstitial space with a different material, such as Ni or Si. The nanospheres can then be removed and more material can be infiltrated to further reduce the porosity (re-infiltration), resulting in a complex network of metallic or semiconductor material. Thus, these types of phononic crystal thin films provide a unique structure with independently adjustable porosity and nanoscale periodicity.

Recent studies have demonstrated that semiconductor metalattices can exhibit tunable thermal transport properties. Specifically, previous theoretical work predicted that semiconductor metalattices with deep nanoscale dimensions can drastically reduce thermal conduction, while possibly leaving electric conduction unaltered, which is optimal for the design of efficient thermoelectric devices.[10,17] More recently, Chen *et al.* predicted and measured the thermal properties of silicon metalattices, both with and without the silica nanosphere template, finding that ballistic phonon behavior dominates in these systems.[12] Moreover, the authors demonstrated that porosity and pore size in metalattices greatly alter both the thermal conductivity and phonon spectrum relevant to thermal transport;[12] therefore, semiconductor metalattices with a tunable geometry and porosity will allow for the development of novel thermal devices.

However, while the primary application of semiconductor metalattices is tailored heat flow, the mechanical properties and porosity of these nanostructured thin films are just as critical for incorporation into devices. If metalattices are potential thermoelectric materials, then they must also possess substantial mechanical strength as poor mechanical properties can lead to device failure and prohibit shrinking device size.[18,19] For example, potential thermoelectric materials such as Bi_2Te_3 and PbTe have poor mechanical properties that limit their applications[19] which has sparked research into enhancing these materials' mechanical properties.[20,21] Additionally, the porosity greatly influences the resulting mechanical and thermal properties of these nanosystems (and is often required as an input by experimental measurement techniques) making it another key parameter to characterize.[12,22]

However, the properties—thermal, mechanical, and structural—of tunable, low-porosity metalattices have not yet been experimentally accessed. Recently, we nondestructively characterized the mechanical and structural properties of silica-filled silicon metalattices, observing that these systems' properties follow continuum predictions.[22] However, both this work and the study by Chen *et al.* exclusively examined semiconductor metalattices with fixed high porosities (or low filling fraction) near the close-packing fraction of hard spheres, where the porosity is known. For low-porosity metalattices fabricated by re-infiltrating semiconductor material after removal of the nanosphere template, the porosity is tunable and cannot yet be predicted or assumed based on the fabrication parameters. Thus, characterizing the porosity will be critical to future studies of tailored heat flow in low-porosity semiconductor metalattices.

Porosity can be extracted by a variety of methodologies, but is especially challenging to measure in porous thin film systems

https://doi.org/10.1021/acsami.2c09360
ACS Appl. Mater. Interfaces 2022, 14, 41316−41327

where the voids may (or may not) be interconnected.[23] Experimental techniques sensitive to porous thin films include, but are not limited to, visible ellipsometry[24] and interferometry,[25] X-ray reflectometry, spectrometry,[26] and scattering,[27] electron microscopy, adsorption porosimetry,[28] ellipsometric porosimetry,[29] and positron annihilation lifetime spectroscopy.[30] Adsorption porosimetry is often considered to be the reference analytical approach; however, thin films are challenging to characterize by this method because it often requires a sufficient quantity of a powdered form of the material.[23,31] Additionally, visible laser-based techniques typically implement effective medium theories which assume a homogeneous material.[23,31] Moreover, approaches that infiltrate a gas or liquid are more suited for systems with interconnected pores, whereas electron microscopy requires cutting electron transparent lamellae from the sample. Thus, nondestructively extracting porosity in thin, nanostructured films with isolated, nanoscale pores is a challenging problem which prohibits the efficient, iterative engineering of nanoscale metalattices. Therefore, better metrology techniques well-suited to probe the mechanical and structural properties of complex, nanostructured systems with feature sizes on the tens of nanometer scale are of paramount importance.

In this work, we harness coherent extreme ultraviolet (EUV) beams to nondestructively extract, for the first time, Young's modulus, film thickness, and porosity of a low-porosity silicon metalattice thin film—a complex 3D nanoscale network with re-infiltrated material resulting in a tunable geometry and interconnectivity which cannot be predicted. We launch nanoscale surface acoustic waves (SAWs) from laser-excited periodic transducer arrays and precisely monitor their dispersion using dynamic EUV scatterometry. The short wavelength of the EUV light allows us to detect short wavelength SAWs in the hypersonic frequency range which are fully confined to the thin silicon metalattice layer. By comparing the measured frequencies to different finite element models of the metalattice structure, we simultaneously extract Young's modulus and porosity, for the first time. By controlling the SAW penetration depth, we also measure the metalattice layer thickness and verify the substrate properties. Additionally, we utilize electron tomography images of a lamella cut from the sample to observe the geometry, porosity, and film thickness, as well as to validate our scatterometry results. This work demonstrates that the correlation and corroboration of advanced characterization techniques is critical for informed and iterative fabrication of devices based on nanostructured metamaterials.

METHODS: SAMPLE FABRICATION

We fabricate thin films of a silicon metalattice with empty pores on the surface of a crystalline silicon substrate. We first synthesize a silica nanosphere template by assembling monodispersed silica nanospheres with sphere radii of 30 nm into a close packed template on a silicon substrate using a vertical deposition technique.[32,33] The parameters of this fabrication technique create a template which varies in thickness (250−2000 nm) across the substrate. We infiltrate the interstitial regions of the silica template with silicon using high-pressure confined chemical vapor deposition[15] until a silicon overlayer is formed to ensure complete filling of the template voids. This overlayer and the silica nanosphere template are removed using reactive ion etching and hydrofluoric acid vapor, respectively. The resulting sample is a high-porosity, empty-pore silicon metalattice with a complex network of larger volumes of silicon, often referred to as "meta-atoms", connected by thin necks called "meta-bonds".[15,22] A unit cell of the high-porosity metalattices is shown in Figure 1a. More fabrication details on these samples can be found in Chen *et al.*[12] In these high-porosity metalattices, the voids can be assumed to be close-packed and thus the porosity and geometry are well-known. However, unlike the previous studies by Chen *et al.*[12] and Abad *et al.*,[22] we re-infiltrate the high-porosity metalattice with silicon using the identical high-pressure confined chemical vapor deposition process for an additional 30 min after the nanosphere template had been removed. This re-infiltration creates a silicon overlayer which we remove using reactive ion etching. We then crystallize the metalattice by annealing, as described in Chen *et al.*[12] This re-infiltration process alters the structure of the metalattice and thus the sample's pore size, porosity, and the interconnectivity of the voids are unknown and require characterization; only the periodicity of the pores remains unchanged during the re-infiltration process. Figure 1a summarizes the fabrication steps.

METHODS: ELECTRON TOMOGRAPHY

To investigate the structure and uniformity of the sample and validate the porosity extraction *via* our dynamic EUV measurement, we perform high-angle annular dark-field scanning transmission electron microscopy (HAADF-STEM) tomography on a focused ion beam prepared lamella of low porosity, that is, re-infiltrated silicon metalattice. After acquiring a single-axis tilt series of the sample, we denoise, align, mask, and bin the images to increase image fidelity, account for sample drift, and reduce the data size. The series of projections is computationally reconstructed *via* the GENFIRE[34] algorithm, resulting in a 3D image of 512 x 512 x 512 voxels. We verify that the resolution of the reconstructed image is limited to the voxel edge length—1.43 nm—*via* Fourier ring correlation analysis with a 1/2-bit threshold as suggested by previous work.[35] To avoid geometric artifacts that arise from the sample geometry, data collection scheme, and Fourier reconstruction method,[36] we crop the reconstructed image to the central 251 x 219 x 125 voxels. Figure 1b displays a slice of the resulting cropped 3D image. See Supporting Information, Section S1 for more details on the electron tomography data acquisition, pre-processing, and reconstruction.

We post-process and segment the resulting 3D image to extract the structure and porosity of the metalattice sample. We perform smoothing and sharpening on individual 2D slices of the 3D tomography data set *via* anisotropic diffusion[37] and unsharp mask sharpening algorithms, respectively, to reduce noise in the image without removing edges.[38] To identify components in the image as silicon or void, we utilize three different segmentation algorithms implemented in MATLAB:[39] global thresholding *via* Otsu's algorithm,[40] local (or adaptive) thresholding,[41] and *k*-means clustering.[42] Figure 1b illustrates the steps in the post-processing procedure. Utilization of different segmentation algorithms allows us to ensure that there are no biases in the analysis as a result of the algorithm choice.[43] Because the scanning transmission electron microscope acquired high-angle annular dark-field images, we note that dark regions in the original reconstruction represent areas of low density. In the segmented reconstruction, regions characterized as silicon are represented by black, whereas voids are indicated by white, as shown in Figure 1b.

We perform further analysis on the reconstructed 3D image and 2D projections to quantify the geometry of the metalattice structure. We verify the periodic pattern of the holes from a 3D Fourier transform. We quantify the periodicity by fitting ellipses to contiguous voids—in both 2D slices of the 3D segmented image and 2D segmented projections before reconstruction—and calculating the separation of the fitted ellipse centroids. We also extract pore size and distribution from these fitted ellipses by calculating the equivalent diameter. Additionally, we extract the pore size and distribution from the 3D images (rather than the 2D projections) by further segmenting the segmented 3D reconstruction to identify individual voids *via* a watershed transform.[44] An algorithm fits ellipsoids to individual voids identified by the watershed transform and we estimate a pore size from the equivalent diameter of the fitted volumes. The 2D projections of the metalattice lamella allow for simple extraction of

https://doi.org/10.1021/acsami.2c09360
ACS Appl. Mater. Interfaces 2022, 14, 41316−41327

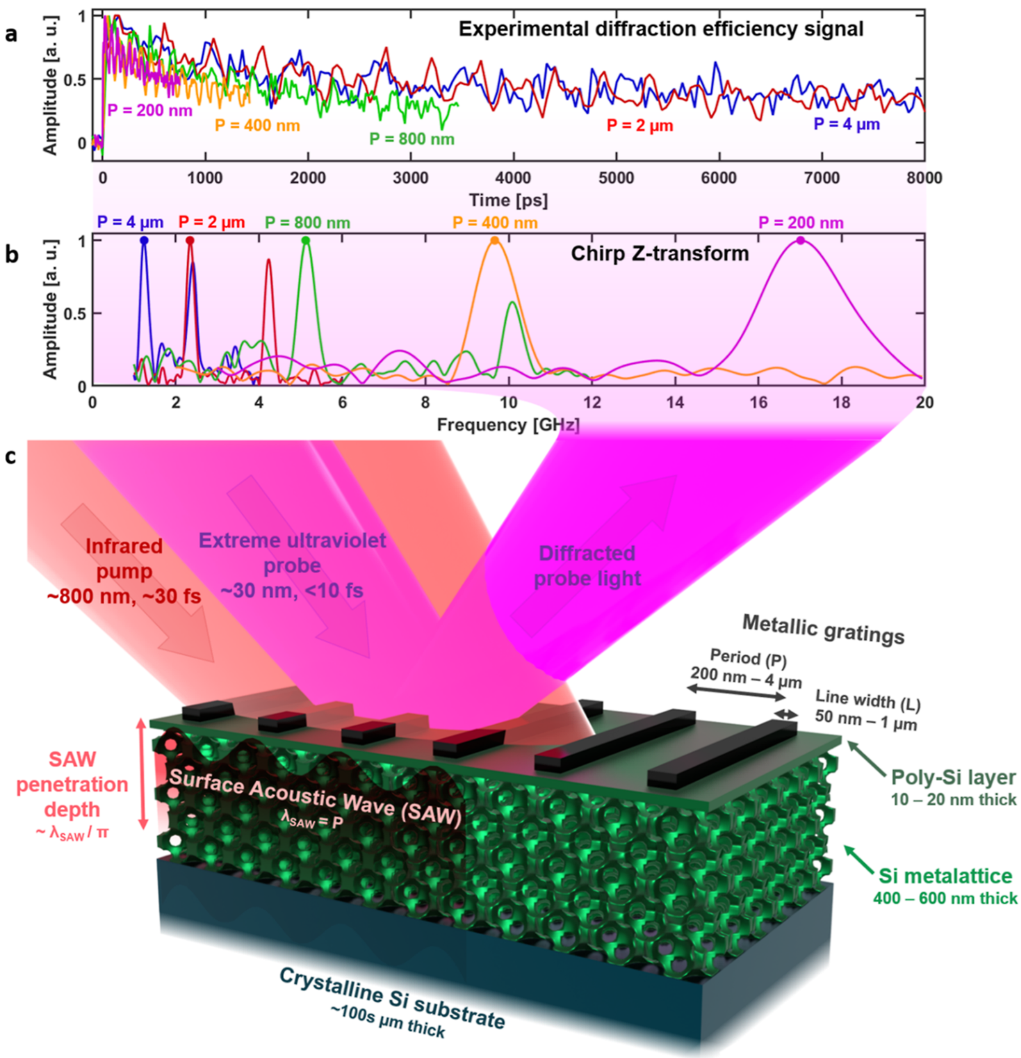

Figure 2. (c) EUV scatterometry accesses SAWs in metalattices. The sample consists of a silicon metalattice layer with 10s of nanometer pores grown on top of a thick crystalline silicon substrate. The surface of the metalattice is covered with a thin 10−20 nm polycrystalline silicon (poly-Si) layer. On the surface of this layer, we fabricate periodic arrays of nickel nanostructures with line widths and periodicities between 50−1000 and 200−4000 nm, respectively. An ultrafast infrared pump pulse, with a wavelength ~800 nm and a ~30 fs pulse duration, directed onto the sample is preferentially absorbed by these metallic gratings, which induces an impulsive thermal expansion launching acoustic waves into the sample below. The resulting SAW has a wavelength (λ_{SAW}) equal to the periodicity of the grating. The SAW penetration depth is $\sim\lambda_{SAW}/\pi$, allowing us to probe different depths in the sample. At a set time delay after the laser pump pulse, an EUV probe pulse with a ~30 nm wavelength and pulse duration <10 fs diffracts from the structured surface. (a) We monitor the change in diffraction efficiency of the EUV beam to detect small surface deformations in the sample and grating induced by the SAWs . (b) A chirp Z-transform of the experimental diffraction signal identifies the precise frequency of the standing SAWs launched by the gratings. Because the SAW wavelength is known and the frequency is measured, the acoustic dispersion can be mapped using gratings of different periodicities, allowing us to access the elastic and structural properties of the sample. We note that some chirp Z-transforms include multiple peaks corresponding to higher harmonics of the fundamental SAW.

the film thickness. By cutting a lamella from the sample at three different positions on the surface, we monitor the variation of the metalattice thickness across the substrate, which arises from the nanosphere assembly process.[32] During this analysis, we observe a thin polycrystalline silicon layer on the surface of the metalattice, which most likely arose from an incomplete removal of the overlayer during the reactive ion etching after the silicon re-infiltration. This layer also varies in thickness across the sample, which we quantify by analyzing the projection images from the three separate lamellae. See Supporting Information, Section S2 for more details on the electron tomography analysis.

METHODS: EUV SCATTEROMETRY

To nondestructively extract the porosity, structural, and elastic properties, we utilize dynamic EUV scatterometry which we previously demonstrated to be a versatile tool in accessing the properties of high-porosity, silica-filled silicon metalattices[22] and ultrathin dielectric films[45] and bilayers.[1] Dynamic EUV scatterometry uses a short-wavelength probe laser to detect hypersonic SAWs, which are selectively sensitive to the near-surface elastic properties. To launch the SAWs, we fabricate periodic arrays of Ni nanolines ranging in line width (L) from 50 to 1000 nm and periodicity (P) from 200 to 4000 nm on the surface of the Si metalattice sample. Our technique possesses similarities to picosecond ultrasonics,[46,47] a versatile visible-laser-based method capable of nondestructive mechanical characterization of thin films independent of substrate properties; however, our technique utilizes a tabletop short-wavelength probe to access SAWs launched by gratings beyond the diffraction limit of visible light. We utilize electron beam lithography to fabricate grating arrays of different geometries on the sample surface (*via* the procedure and

https://doi.org/10.1021/acsami.2c09360
ACS Appl. Mater. Interfaces 2022, 14, 41316−41327

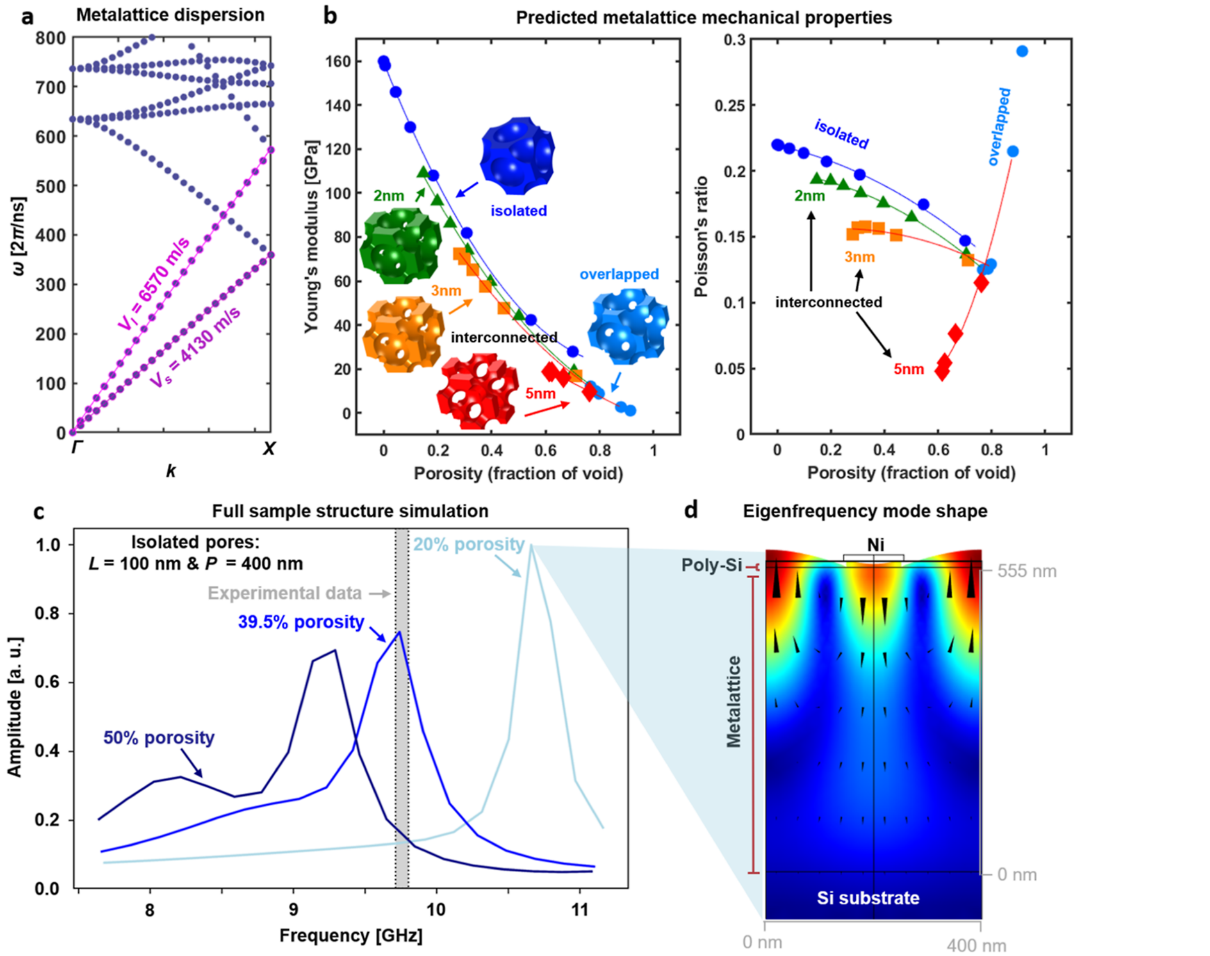

Figure 3. (a) Metalattice dispersion calculation. We use FEA to calculate the metalattice dispersion by computing the modal eigenfrequencies (ω) of the unit cell with a varying wavevector (k). The longitudinal (V_l) and shear (V_s) acoustic wave velocities can be extracted by a linear fit of the lowest order branches. (b) Predicted metalattice elastic properties. We predict Young's modulus and Poisson's ratio as a function of porosity, for different metalattice geometries. We simulate five different models of the geometry: (i) an isolated model with entirely separate spherical voids (dark blue at low porosity), (ii) an overlapped model with overlapping spherical voids (light blue at high porosity), and an interconnected model where separate spherical voids are interconnected with perfect cylindrical channels of varying radius—(iii) 2 nm (green), (iv) 3 nm (orange), and (v) 5 nm (red). At sufficiently high porosity, all interconnected models limit to the overlapped model when the spherical overlap diameter is greater than the cylindrical interconnection diameter. Additionally, the porosity for the interconnected model is limited when the geometry is entirely composed of cylinders. (c) SAW-likeness of full sample structure simulations. We calculate the observed SAW frequency *via* a full sample structure simulation. In this example, we show the SAW-likeness curves for a grating geometry with a nominal line width (L) of 100 nm and a nominal period (P) of 400 nm with elastic properties specified by the isolated pores curve from (b) with porosities of 20% (light blue), 39.5% (blue), and 50% (dark blue). In this case, a porosity of 39.5% is the best fit to the experiment, as the SAW-likeness peak matches the experimentally extracted frequency (gray bar). (d) Eigenfrequency mode shape. We display the SAW mode shape corresponding to the peak value of the SAW-likeness metric for a grating with $L \approx 100$ nm and $P \approx 400$ nm on a 20% porosity, isolated pores metalattice model. The colors indicate the magnitude of the displacement on an arbitrary scale. We note that the SAW energy (which is related to the square of the displacement) is confined to the surface and within the metalattice film.

methods detailed in Supporting Information of ref 22). We verify the nanoline array geometries, that is, L, P, and height, *via* atomic force microscopy (AFM), as shown in Supporting Information, Section S3.

An ultrafast, infrared laser pump pulse with a wavelength of ~800 nm and a pulse duration of ~30 fs is incident on the sample surface at a 45° angle, where it is preferentially absorbed by the metallic gratings (see Figure 2c for the setup). The pump laser induces a rapid heating accompanied by an impulsive thermal expansion. This coherent excitation of periodic structures launches a SAW with wavelength (λ_{SAW}) set by the period of the grating. The SAW penetration depth (δ_{SAW}) and thus its sensitivity to near-surface properties, is directly related to its wavelength as $\delta_{SAW} \sim \lambda_{SAW}/\pi$.[48] Therefore, by controlling the periodicity of the nanostructure arrays, we directly alter the depth sensitivity of the acoustic waves, that is, large period gratings are predominantly sensitive to the substrate properties, whereas short period gratings are only sensitive to the metalattice properties.[22,45]

To observe the SAWs, a coherent EUV probe beam monitors the temporal evolution of the surface displacement caused by the acoustic waves. We generate the EUV beam by focusing ~1 mJ, 30 fs infrared pulses (derived from the same laser as the pump beam) into a hollow-core capillary filled with 30 Torr of Ar. An extreme quantum nonlinear process known as high harmonic generation upconverts the infrared light into coherent beams of ~30 nm wavelength and <10 fs pulse duration.[49] The short wavelength of these probe pulses is exquisitely sensitive to picometer displacements of the surface[50] and can scatter from acoustic waves with wavelengths of 10s of nanometers.[51] An EUV-sensitive CCD camera collects the probe light diffracted from the dynamically deforming sample surface, while a mechanical stage controls the time delay between the pump and probe pulses (see Figure 2c for a schematic of the setup).

https://doi.org/10.1021/acsami.2c09360
ACS Appl. Mater. Interfaces 2022, 14, 41316−41327

By analyzing the time-dependent diffraction of the EUV probe beam off of the dynamic surface deformation, we can directly measure the frequency of hypersonic SAWs with penetration depths set by the various grating periods. By aggregating CCD images of the probe diffraction, we compute the normalized change in diffraction efficiency[52] as a function of time delay, which is plotted in Figure 2a for five different nanoline grating periods: $P = 4000$ nm, $P = 2000$ nm, $P = 800$ nm, $P = 400$ nm, and $P = 200$ nm. The oscillations in these time signals correspond to oscillations in the surface displacement induced by the propagating SAWs. We compute a chirp Z-transform, a generalization of the discrete Fourier transform along a contour that is not the unit circle, of these time traces, which is shown in Figure 2b. The highest amplitude/lowest frequency peaks in each transform indicate the fundamental SAW frequency ($\lambda_{SAW} = P$), whereas the smaller amplitude/higher frequency peaks arise from higher harmonics of the fundamental SAW (because the excitation is not purely sinusoidal). We note that the higher frequency peaks tend to be broader due to the higher damping of the SAW because the acoustic wave is more strongly scattered by the grating.[53,54] We know the wavelength of the fundamental SAW, as it is set by the periodicity of the grating. We confirm this by observing that the first EUV diffraction order predominantly contains the fundamental SAW temporal frequency, indicating that the spatial frequency of the wave is identical to that of the grating. Thus, we extract the SAW dispersion from wavelengths of 4 μm to 200 nm and relate it to the properties of the sample, including film thickness, porosity, and material elastic properties.

METHODS: THERMOMECHANICAL MODELING

To extract structural and elastic properties of the sample from the SAW dispersion, we must first create models of the metalattice and full sample structure. A previous study by do Rosário *et al.* performed finite element analysis (FEA) simulations to predict the mechanical properties of samples with similar structure as the ones in this study.[55] Additionally, our previous work on silica-filled, high-porosity metalattices indicated that although these structures contain nanoscale features, their macroscale mechanical properties follow continuum predictions by FEA models.[22] Thus, we utilize FEA calculations implemented in COMSOL[56] to predict the elastic properties of these low-porosity, empty metalattice structures. Because the geometry of the pore interconnectivity within the metalattice is not precisely known, we construct three different models of the metalattice structure: isolated pores, interconnected pores, and overlapped pores. The isolated model consists of spherical pores arranged in a face-centered cubic (FCC) geometry, which is expected from the fabrication and validated by the electron tomography, whereas the interconnected model is identical to the isolated model except with cylindrical channels of void connecting the centers of the nearest neighbor pores. If the diameter of the pores in the isolated or interconnected model is increased sufficiently, the pores will overlap (eventually the connecting hole diameter will be larger than the channel diameter), creating a network of overlapping voids which we denote as the overlapped model. Thus, the overlapped geometry is just a limiting case of the isolated and interconnected models at large pore diameters.

We implement these different models of metalattice interconnectivity geometry (visualized in Figure 3) into our FEA simulations to calculate the acoustic wave dispersion for a metalattice that extends infinitely in all directions. We construct a single unit cell with a fixed side length, as the dispersion calculation is insensitive to the absolute value of the periodicity, subject to Bloch boundary conditions on all sides (see Supporting Information, Section S4). We set the elastic properties of the material to that of polycrystalline silicon (Young's modulus = 160 GPa, Poisson's ratio = 0.22, and density = 2330 kg/m^3)[57−59] which was shown to be a good approximation in our previous work.[22] To compute the dispersion, we then search for the lowest modal eigenfrequencies (ω) of the simulation geometry at many different values of $\vec{k}$, sweeping from the Γ-point to the X-point of the FCC metalattice structure. We plot the obtained ω's as a function of $\vec{k}$ as shown in Figure 3a. To compute the elastic properties from the dispersion, we apply a linear fit to the lowest two separate branches of the dispersion (note that the lowest branch is actually degenerate along this direction of k-space). The slopes of the higher and lower branches give us the longitudinal (V_l) and shear (V_s) wave velocities, respectively. The effective Young's modulus and Poisson's ratio of the material system can be expressed in terms of acoustic wave velocities and the metalattice density (see Supporting Information, Section S4), where the density is equal to unity minus the porosity, p, all multiplied by the polycrystalline silicon density. The porosity can be computed analytically for the overlapped geometries from the following equations

$$p_{\text{overlapped}} = \frac{\pi}{3\sqrt{2}}\left(\frac{6\left(1+\frac{1}{2}\left(\frac{d}{D}\right)^2\right)\left(1-\left(\frac{d}{D}\right)^2\right)^{1/2} - 5}{\left(1-\left(\frac{d}{D}\right)^2\right)^{3/2}}\right) \tag{1a}$$

and

$$a^2 = 2(D^2 - d^2) \tag{1b}$$

where D is the pore diameter, d is the diameter of the hole created by the overlap, and a is the unit cell size (see Supporting Information, Section S5 for derivation). For the isolated geometries, the porosity can be computed from the trivial equation

$$p_{\text{isolated}} = \frac{16\pi}{3a^3}\left(\frac{D}{2}\right)^3 \tag{2}$$

and, for the interconnected geometries, the porosity is directly calculated from the FEA model.

Using this method, we compute the elastic properties as a function of porosity for five different models as shown in Figure 3b. To vary the porosity, we adjust the pore diameter size, D. We simulate an isolated pores model (blue) from a pore diameter size of 0 to just before the pores become overlapped, resulting in a large range of achievable Young's moduli (160−28 GPa). We also compute the elastic properties for three different interconnected models: 2 nm (green), 3 nm (orange), and 5 nm (red) radius channels. For each interconnected model, we sweep porosity by varying the pore diameter while holding the channel radius constant. Because we hold the channel radius constant, a minimum achievable porosity occurs at the point where the pore diameter equals the channel diameter. Thus, for the interconnected models, there is a maximum possible Young's modulus which depends on the channel radius used. Once the pore diameter becomes sufficiently large, the interconnected and isolated models limit to the overlapped model (light blue) resulting in the most compliant material. Note that if the pore size is increased too far, the silicon is no longer interconnected, which is not a physically realizable situation. To obtain finer resolution on the relation between the elastic properties and porosity, we interpolate the results by fitting a quadratic polynomial with an argument of $(1 - p)$ because the elastic properties of porous silicon often follow a power-law scaling, as shown by previous studies[60,61] (see Supporting Information, Section S6 for interpolation equations).

For a SAW propagating on a semi-infinite substrate, Young's modulus and Poisson's ratio are analytically related to the measured frequency.[48] However, the periodic nanolines which launch the SAWs also perturb their velocity (due to mass loading of the surface, the elastic stiffness of the nanolines, and the interface bonding properties), in addition to alterations caused by the finite thickness of the metalattice and the presence of a silicon overlayer.[48,53,54,62] Therefore, we implement an FEA model of an entire period of the full sample structure including the nanoline geometry, a silicon overlayer, a native oxide layer, a finite thickness homogeneous film of effective properties representing the metalattice, and the crystalline silicon substrate, as shown in Figure 3d. We use the quantitative relations between the elastic properties and porosity for the different metalattice models as shown in Figure 3b as inputs for the homogeneous film that represents the metalattice in the full sample

https://doi.org/10.1021/acsami.2c09360
ACS Appl. Mater. Interfaces 2022, 14, 41316−41327

structure simulations. We also utilize AFM measurements to accurately model the nanoline height, line width, and periodicity. Additionally, we use nominal literature properties for the 1−2 nm native oxide layer and the silicon overlayer, whose thickness we estimate from the electron tomography data.[57−59,63−65] We apply periodic boundary conditions to the sides of each layer, a fixed boundary condition on the substrate bottom, and free boundaries on the top surface to accurately match the physical experiment. Because we cannot model a semi-infinite substrate directly, we use a sufficiently large depth of 20 μm and validate that increasing the depth does not appreciably alter the results.

We compare the simulated fundamental SAW frequencies in the full sample structure to those measured in our experiments to extract the properties of the metalattice. We vary the parameter we wish to extract—such as porosity—in the simulation and compute several hundred of the resulting modal eigenfrequencies for every value of that parameter. To identify which eigenfrequency is the fundamental SAW observed in the experiment, we perform an efficient computation of the SAW-likeness coefficient as defined by Nardi *et al.* which essentially measures the localization of acoustic energy at the surface.[53] Removing the antisymmetric eigenfrequency modes as they will not be launched by a uniform excitation of the nanostructures, we plot the SAW-likeness coefficient as a function of the modal frequency, as shown in Figure 3c; the resulting peak corresponds to the frequency of the fundamental SAW (we note that the discretization of the eigenfrequencies is a result of the finite thickness of the substrate). Each value of the parameter considered produces a peak in the SAW-likeness coefficient at a specific frequency; when this simulated peak and measured experimental SAW frequencies agree, we know that the values for material properties and sample geometry used in the simulation are capable of reproducing the experiment. In Figure 3d, we display an example of the eigenfrequency mode shape corresponding to the fundamental SAW, illustrating the periodic surface displacement detected by our experiment and the finite penetration depth of the acoustic wave energy for a grating with $L \approx$ 100 nm and $P \approx$ 400 nm. We also use this procedure to check the sensitivity of simulated frequencies to various input parameters, allowing us to propagate errors through the calculations as detailed in Supporting Information, Section S7.

While the SAW-likeness coefficient calculation is efficient, it identifies all eigenmodes which are confined to the surface, including longitudinal and higher order modes which only weakly or negligibly contribute to the EUV diffraction signal and thus this SAW-likeness method cannot be exclusively relied upon to identify the fundamental SAW mode observed in the experiment. To validate the SAW-likeness method, we perform a more computationally intensive projection calculation as detailed by Nardi *et al.*[54] In this case, we simulate the time-dependent evolution of the nanostructure after excitation to resolve the precise profile of the system at maximal thermal expansion. We then decompose this initial excitation onto the modal eigenfrequency basis and calculate projection coefficients, which quantify the prominence of each mode in the simulated excitation. To further confirm that the identified frequency matches that of the experiment, we run a time-dependent simulation of the excited nanostructure to observe multiple temporal oscillations of the acoustic wave, a computationally expensive calculation, and model the light diffraction from the surface. In identical fashion to the experiment, we perform a chirp Z-transform on the modeled change in diffraction efficiency. In both the projection calculation and the time-dependent simulation, we find prominent peaks in agreement with the more computationally efficient SAW-likeness method, as shown in Supporting Information, Section S8.

■ RESULTS: ELECTRON TOMOGRAPHY

The analyzed electron images, both raw 2D projections and 3D tomographic reconstructions, provide information on the metalattice porosity, geometry, and thickness over a localized area. We extract the porosity from a segmented 3D tomographic image as shown in Figure 4, where the visualized

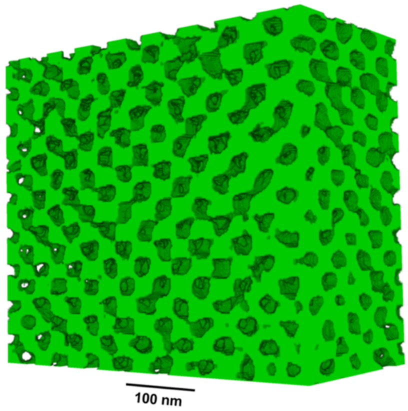

Figure 4. HAADF-STEM tomography reconstruction of a silicon metalattice. We reconstruct a 3D image of a silicon metalattice from a HAADF-STEM tomographic tilt series. The reconstructed image is then segmented using global thresholding to distinguish voids from silicon (green volume) and visualized *via* software *tomviz*.[66] The tomography data reveal the periodic pores in a FCC arrangement with sizes and periodicities on the 10s of nanometer scale. We note that some of the voids appear interconnected, whereas others are isolated. The voxels of the reconstructed image are 1.4 nm. The percentage of voids, or porosity, is 38−42% where the error represents the variance in outputs from the different algorithms.

green volume represents the identified silicon. Movies of the tomographic reconstruction before and after segmentation are available in the Supporting Information. By counting the fraction of void voxels in the tomographic image, we compute the porosity to be 40 ± 2%, where the error arises from variations in the three different segmentation algorithms used (*i.e.*, *k*-means resulted in the highest porosity, whereas local thresholding obtained the lowest). A Fourier transform of the reconstructed images before segmentation yields a body-centered cubic pattern in Fourier space, indicating that the pores have the expected FCC structure in real space (see Supporting Information, Section S2). The periodicity of this FCC structure is 35−36 nm, which we determine by computing the distance between ellipse centroids fitted to the segmented voids in the 2D electron projections as described in Methods: Electron Tomography. We also calculate the diameter and distribution of the pores in the metalattice; however, due to imperfections and the complexities of the pores' interconnections, precise quantification is challenging. We estimate that the average pore size is 10−20 nm based on the equivalent diameter calculation described in Methods: Electron Tomography (see Supporting Information, Section S2 for plotted distributions). Due to the irregularity of the metalattice structure as shown in Figure 4, the ellipse fitting process or the watershed segmentation will often misidentify a single pore (and its interconnections) as multiple pores, or *vice versa*. Essentially, the ambiguity in defining the boundary between a pore and its interconnection precludes a more precise quantification of the pore size and interconnectivity, that is, the percentage of voids that are connected to other voids. We note that setting D = 20 nm and a = 35 nm in eq 2 for isolated geometries implies that the porosity is ∼39%, which agrees with the measured porosity. Therefore, if the contiguous void regions defined as "pores" are close to 20 nm in diameter, then most of the void volume arises from the pores, and if the pore diameters are close to 10 nm, then most of the void volume arises from the interconnections.

https://doi.org/10.1021/acsami.2c09360
ACS Appl. Mater. Interfaces 2022, 14, 41316−41327

From the cut lamellae, we also measure the film and silicon overlayer thickness at three different positions across the sample. We find that the thickness of the sample varies linearly across the surface with thicknesses ranging from 398 ± 4 to 612 ± 3 nm. The thickness of the silicon layer also varies across the sample in inverse relation to the metalattice thickness, that is, it is thicker when the metalattice is thinner and *vice versa*. We observe that this layer ranges from 19 ± 2 to 10 ± 4 nm.

The complexity of this sample demonstrates the imperative need for more and better metrology techniques in correlative measurements. Not only is the metalattice structure complex and irregular but the metalattice is also a thin film which varies in thickness across the substrate surface in addition to an oppositely varying silicon overlayer. The 3D electron tomographic images at different positions on the sample allow us to independently validate the metalattice porosity, pore geometry, periodicity, pore size, and thickness. Although electron microscopy can provide much of the necessary information in a destructive manner, the measurement is lengthy, the reconstruction requires enormous computational power, and the analysis is challenging. Therefore, metrology techniques to nondestructively measure layer thicknesses and porosities averaged over large areas, in addition to mechanical properties, are critical for the iterative design of novel metamaterials for new technologies.

■ RESULTS: DYNAMIC EUV SCATTEROMETRY

Using dynamic EUV scatterometry in conjunction with FEA models of the metalattice and full sample structures, we nondestructively extract the porosity, Young's modulus, Poisson's ratio, and thickness of the metalattice film along with variations in the substrate properties. To extract the properties of metalattice film independently of the substrate, we utilize data collected on two grating geometries: L = 100 nm with P = 400 nm and L = 50 nm with P = 200 nm. These gratings launch SAWs which are predominantly confined to the metalattice film and relatively insensitive to the film thickness and substrate properties. Employing the isolated pores model, we find an average porosity fit of 38.5 ± 2.0%, which is in good agreement with the results from electron tomography, as shown in Figure 5a. Specifically, we extract a porosity of 35.7–40.2 and 36–44.5% for the P = 400 nm and P = 200 nm grating geometries, respectively. With the 2 nm channel interconnected model, we observe porosity fits that are lower than the isolated model and tomography results, as shown in Figure 5a. Interestingly, the 3 and 5 nm channel interconnected models along with the overlapped pores model either produce unphysical results or cannot be fit to the experimental data because these models are limited in the material properties achievable. The error bars on the porosity fits include uncertainty in the grating geometry, material properties, layer thicknesses, and experimental data (see Supporting Information, Section S7 for more details on error bar calculations). The porosity uncertainty is dominated by error in the experimental measurement of the SAW frequency and grating periodicity, while error in other input parameters, such as grating line width and oxide layer thickness, does not significantly affect the results. The porosity values extracted from the P = 200 nm data have higher error bars because the SAW is more sensitive to the precise metalattice thickness due to stronger coupling to bulk longitudinal acoustic waves within the film and because the uncertainty in metalattice thickness for these gratings is higher. Using the quadratic fits from Figure 3b, we can extract the elastic properties of the metalattice layer in the isolated model, finding Young's modulus equal to 67 ± 4 and 64 ± 7 GPa for P = 400 nm and P = 200 nm, respectively, as shown in Figure 5b. Interestingly, we observe that the

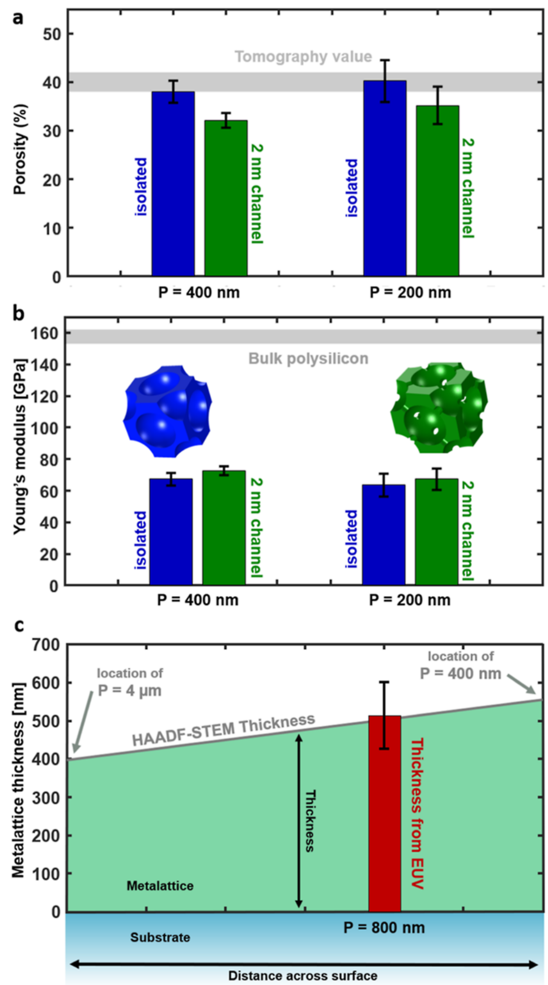

Figure 5. (a) Extracted porosity values. Using equations fit with the isolated model, the extracted porosities from the P = 400 nm and P = 200 nm gratings—where SAWs are fully confined to the metalattice film—agree well with the porosity value extracted from the tomography data. The 2 nm radius channel model results in porosity values somewhat lower than the isolated model; however, they are still reasonably close to the tomography value. The P = 200 nm extracted porosity has larger bounds due to increased experimental error and the uncertainty on the metalattice thickness. Thus, our experimental measurements combined with finite element models can nondestructively extract average porosity over larger areas than tomography. (b) Extracted Young's modulus values. We also extract Young's modulus and Poisson's ratio (see Supporting Information, Section S9 for the latter). We note that the extracted Young's modulus is more similar between the two reasonable models (isolated and 2 nm channels) than the extracted porosity values. (c) Extracted thickness. We extract the metalattice thickness using the experimental data from the P = 800 nm periodic grating, where the SAW propagates partially in the silicon substrate. We find a best fit thickness of ~500 nm. The thickness variation across the sample due to the fabrication technique as extracted from HAADF-STEM images is approximately plotted (gray line) and we find that if a linear variation between measurements is assumed, our extracted value matches well. We note that the x-axis represents physical distance across the sample surface in ~350 μm increments.

https://doi.org/10.1021/acsami.2c09360
ACS Appl. Mater. Interfaces 2022, 14, 41316–41327

Young's modulus extracted using the 2 nm channel interconnected model is quite similar to the result of the isolated model even though the extracted porosity result is dissimilar. Furthermore, we note that these values for the metalattice Young's modulus are similar to Young's modulus measurements of bulk mesoporous silicon at the same porosity (~60 GPa at 40% porosity), where pores on a 2−50 nm scale are randomly distributed and interconnected, creating a significantly different structural geometry than a metalattice.[65] The extracted values and error bars for Poisson's ratio of the metalattice, which we simultaneously extract with Young's modulus, lie between 0.177 and 0.193 (see Supporting Information, Section S9 for more details); however, our sensitivity to the precise value of Poisson's ratio is lower than that of Young's modulus.

The porosity value extracted using the isolated pores model is in excellent agreement with the value calculated from the electron tomography reconstruction, demonstrating that the EUV scatterometry technique, when coupled with physical models, can be used to nondestructively extract the porosity of thin films. As mentioned above, the 2 nm channel interconnected model results in lower porosity values which do not match the electron tomography as well. We recognize that the tomography images in Figure 4 illustrate that the metalattice is not as perfectly uniform as assumed by the models, especially in regards to the interconnections. To investigate this further, we perform calculations with two more models of the metalattice structure: we take the 2 nm channel interconnected model with 50 or 75% of the channels randomly removed, as discussed in Supporting Information, Section S10. We find that these models produce Young's modulus *versus* porosity curves between the 2 nm channel interconnected (green) and isolated (blue) model curves in Figure 3b. The results are not sensitive to precisely which channels have been removed. Thus, the acoustic wave dispersion at longer wavelengths is relatively insensitive to the precise details of the interconnection structure, implying that volume reduction has a more dominant influence over the long-wavelength acoustic velocity than scattering by internal surfaces. Moreover, our experimental measurements occur over a ~100 μm × 100 μm area and thus average over imperfections within the metalattice structure. Therefore, the better agreement of the isolated pores model may imply that these metalattices are, on average, better approximated by isolated holes, while the 100% interconnectivity of 2 nm radius channels is an overestimate of the true metalattice interconnectivity. In other words, we suspect that the average sample interconnection channel diameter is closer to zero than to 4 nm (a diameter of zero implies no interconnection). As previously discussed, the ambiguity in identifying a "pore" *versus* an "interconnection" causes us to be unable to validate this conclusion with the electron tomography data. In summary, if one *a priori* knows, or can determine, a reasonable geometrical model for the actual metalattice sample structure, dynamic EUV scatterometry can be used to nondestructively extract the elastic properties and porosity of thin films.

If an appropriate model of the metalattice, or a different nanostructured material, is not available or cannot be determined, our technique can still be used to nondestructively extract the elastic properties. This capability has applications well beyond metalattices, extending to mechanical characterization of more general, complex nanostructured films, such as nanogranular thin films that have been studied by ultrafast optoacoustic techniques.[67,68] We demonstrate characterization without a metalattice structural model by using the porosity values obtained from electron tomography as direct inputs into the simulation. In this situation, we do not need to use a model of the metalattice structure (in particular, we do not need the results of Figure 3a,b); the porosity determines the density, whereas Poisson's ratio can be assumed because it has much lower sensitivity than Young's modulus, as seen from Figure 3b. Thus, the only unknown is Young's modulus and we can directly fit it, as done in ref 22, finding a result of 66 and 64.5 GPa for P = 400 nm and P = 200 nm, respectively, independent of any assumptions on metalattice structure. This result is in excellent agreement with our extraction of both elastic properties and porosity using the dispersion calculations, lending validity to our approach. Moreover, we note that these results are in closer agreement with the isolated pores model than the 2 nm interconnected pores model, further confirming our deduction that the former is more representative of the physical sample. Essentially, the dispersion calculations and varying structure models as shown in Figure 3a,b package the elastic properties and density into a single parameter p, or porosity, which can be easily extracted from the data.

Not only can our technique extract the elastic properties and porosity of the metalattice, it can also determine metalattice thickness and the substrate properties. The grating with L = 100 nm and P = 800 nm, where significant acoustic energy propagates in both the metalattice and substrate, is most sensitive to the thickness. We simulate a grating of this geometry with the metalattice properties set by the porosity extracted from the smaller period gratings and vary the thickness. We find the best agreement with experimental data when the metalattice thickness is 515 ± 87 nm, where the error bar arises from experimental uncertainty and uncertainties in other simulation input parameters. Using cross-sectional electron microscopy images, we measured the metalattice thickness at three different locations across the sample, finding a roughly linear variation (see Supporting Information, Section S1 for a sample layout). The P = 800 nm grating lies between two of our cross-sectional measurements and a linear interpolation predicts that the thickness under this grating should be ~500 nm, which is in excellent agreement with the EUV scatterometry results as illustrated in Figure 5c. Finally, we can use the two largest period gratings, P = 2000 nm and P = 4000 nm, to fit the silicon substrate properties, as the SAWs launched from these gratings are relatively insensitive to small changes in the metalattice properties and thickness. We find that a silicon substrate orientation of (100) fits the data at both large grating periodicities well. Although the fits for the P = 4000 nm precisely agree with the literature, we observe that the elastic tensor fits for P = 2000 nm are slightly more compliant. We hypothesize that this is due to strain localized near the film−substrate interface, to which the smaller period grating will be more confined and more sensitive (for more details, see Supporting Information, Section S11).

■ CONCLUSIONS

In summary, we utilize electron tomography to probe the void geometry and porosity, and dynamic EUV scatterometry to nondestructively extract the porosity, Young's modulus, Poisson's ratio, and thickness of low-porosity silicon metalattice thin films. Using our coherent, short-wavelength probe pulses, we detect SAWs with nanometer-scale penetration

https://doi.org/10.1021/acsami.2c09360
ACS Appl. Mater. Interfaces 2022, 14, 41316−41327

depths, whose dispersion is sensitive to film properties and thickness. By constructing continuum models of the metalattice structure, we link the porosity to the elastic properties to extract all parameters simultaneously and find that an isolated pores model represents these metalattices better than pores interconnected by channels with radius ≥2 nm. We include effects of a native oxide layer, silicon overlayer, and finite film thickness into our models and find excellent agreement with measurements made by electron tomography and cross-sectional electron microscopy. Moreover, our measurement approach could be adapted to ultrathin, complex nanostructured films beyond metalattice films, even where details on the nanostructuring are unknown and bulk theoretical models fail, such as ultrathin nanoparticle films. This work demonstrates that combined and correlative measurements of complex, nanostructured samples with feature sizes on the 10 nm scale and below are critical for the progress of new nano- and quantum technologies.

■ ASSOCIATED CONTENT

Supporting Information

The Supporting Information is available free of charge at https://pubs.acs.org/doi/10.1021/acsami.2c09360.

Electron tomographic measurements and reconstruction, analyzing HAADF-STEM images, AFM results, more details on unit cell dispersion calculations, derivation of porosity equation for overlapped geometry, quadratic fits of the metalattice properties for different geometries, procedure for error bar calculation, validation of the SAW-likeness coefficients, extracted Poisson's ratio of the metalattice, predicted effects of removing interconnections on the metalattice properties, extraction of substrate properties, and multimedia objects of the metalattice structure in online version (PDF)

HAADF-STEM tomographic reconstruction (AVI)

HAADF-STEM tomographic reconstruction with segmentation (AVI)

■ AUTHOR INFORMATION

Corresponding Author

Joshua L. Knobloch − *Department of Physics, JILA, and STROBE NSF Science & Technology Center, University of Colorado and NIST, Boulder, Colorado 80309, United States;* orcid.org/0000-0002-4086-3746; Email: joshua.knobloch@colorado.edu

Authors

Brendan McBennett − *Department of Physics, JILA, and STROBE NSF Science & Technology Center, University of Colorado and NIST, Boulder, Colorado 80309, United States*

Charles S. Bevis − *Department of Physics, JILA, and STROBE NSF Science & Technology Center, University of Colorado and NIST, Boulder, Colorado 80309, United States;* Present Address: Department of Physics, University of Pavia, Pavia, Italy

Sadegh Yazdi − *Renewable and Sustainable Energy Institute and the Materials Science & Engineering Program, University of Colorado, Boulder, Colorado 80309, United States;* orcid.org/0000-0002-3470-9398

Travis D. Frazer − *Department of Physics, JILA, and STROBE NSF Science & Technology Center, University of Colorado and NIST, Boulder, Colorado 80309, United States;* Present Address: Argonne National Laboratory, Lemont, Illinois.; orcid.org/0000-0002-5162-4230

Amitava Adak − *Department of Physics, JILA, and STROBE NSF Science & Technology Center, University of Colorado and NIST, Boulder, Colorado 80309, United States;* Present Address: Department of Physics, Indian Institute of Technology (Indian School of Mines), Dhanbad, India.; orcid.org/0000-0003-0687-2830

Emma E. Nelson − *Department of Physics, JILA, and STROBE NSF Science & Technology Center, University of Colorado and NIST, Boulder, Colorado 80309, United States;* orcid.org/0000-0003-4336-3242

Jorge N. Hernández-Charpak − *Department of Physics, JILA, and STROBE NSF Science & Technology Center, University of Colorado and NIST, Boulder, Colorado 80309, United States;* Present Address: American Physical Society.; orcid.org/0000-0003-3296-6929

Hiu Y. Cheng − *Department of Chemistry and Materials Research Institute, The Pennsylvania State University, University Park, Pennsylvania 16802, United States*

Alex J. Grede − *Department of Chemistry and Materials Research Institute, The Pennsylvania State University, University Park, Pennsylvania 16802, United States*

Pratibha Mahale − *Department of Chemistry, University of Pennsylvania, Philadelphia, Pennsylvania 19104, United States*

Nabila Nabi Nova − *Department of Chemistry and Materials Research Institute, The Pennsylvania State University, University Park, Pennsylvania 16802, United States*

Noel C. Giebink − *Department of Chemistry and Materials Research Institute, The Pennsylvania State University, University Park, Pennsylvania 16802, United States;* orcid.org/0000-0002-3798-5830

Thomas E. Mallouk − *Department of Chemistry, University of Pennsylvania, Philadelphia, Pennsylvania 19104, United States*

John V. Badding − *Department of Chemistry and Materials Research Institute, The Pennsylvania State University, University Park, Pennsylvania 16802, United States*

Henry C. Kapteyn − *Department of Physics, JILA, and STROBE NSF Science & Technology Center, University of Colorado and NIST, Boulder, Colorado 80309, United States; KMLabs Incorporated, Boulder, Colorado 80301, United States*

Begoña Abad − *Department of Physics, JILA, and STROBE NSF Science & Technology Center, University of Colorado and NIST, Boulder, Colorado 80309, United States;* Present Address: Department of Physics, University of Basel, Basel, Switzerland.; orcid.org/0000-0001-7589-7973

Margaret M. Murnane − *Department of Physics, JILA, and STROBE NSF Science & Technology Center, University of Colorado and NIST, Boulder, Colorado 80309, United States*

Complete contact information is available at: https://pubs.acs.org/10.1021/acsami.2c09360

Author Contributions

M.M.M., H.C.K., and J.V.B. conceived the experiment. J.L.K., T.D.F., B.A., A.A., and J.N.H.-C. carried out the EUV scatterometry measurements. J.L.K., T.D.F., B.A., A.A., and B.M. analyzed the EUV scatterometry data. P.M. fabricated the nanosphere templates. H.Y.C. fabricated the metalattices. A.J.G. fabricated the nanoline gratings. B.A. and T.D.F. performed the AFM measurements. S.Y. performed the electron microscopy. C.S.B. reconstructed the tomography data. J.L.K. constructed and performed the metalattice dispersion simulations. J.L.K., B.M., and E.E.N. constructed and performed the FEA simulations for the full sample. All authors discussed the results and either wrote or reviewed the paper.

Notes

The authors declare no competing financial interest.

■ ACKNOWLEDGMENTS

The authors gratefully acknowledge support from the STROBE National Science Foundation Science & Technology Center, grant no. DMR-1548924, for the setups and methods, and the Penn State Center for Nanoscale Science, an NSF-sponsored Materials Science and Engineering Center under award DMR-1420620, for synthesizing the samples. Support from the Facility for Electron Microscopy of Materials (CU FEMM, RRID: SCR_019306) is acknowledged.

■ REFERENCES

(1) Frazer, T. D.; Knobloch, J. L.; Hernández-Charpak, J. N.; Hoogeboom-Pot, K. H.; Nardi, D.; Yazdi, S.; Chao, W.; Anderson, E. H.; Tripp, M. K.; King, S. W.; Kapteyn, H. C.; Murnane, M. M.; Abad, B. Full Characterization of Ultrathin 5-nm Low-*k* Dielectric Bilayers: Influence of Dopants and Surfaces on the Mechanical Properties. *Phys. Rev. Mater.* **2020**, *4*, 073603.

(2) Han, J. E.; Crespi, V. H. Abrupt Topological Transitions in the Hysteresis Curves of Ferromagnetic Metalattices. *Phys. Rev. Lett.* **2002**, *89*, 197203.

(3) Han, J. E.; Crespi, V. H. Tuning Fermi-Surface Properties through Quantum Confinement in Metalattice: New Metals from Old Atoms. *Phys. Rev. Lett.* **2001**, *86*, 696.

(4) Meza, L. R.; Das, S.; Greer, J. R. Strong, Lightweight, and Recoverable Three-Dimensional Ceramic Nanonolattices. *Science* **2014**, *345*, 1322.

(5) Hoogeboom-Pot, K. M.; Hernandez-Charpak, J. N.; Gu, X.; Frazer, T. D.; Anderson, E. H.; Chao, W.; Falcone, R. W.; Yang, R.; Murnane, M. M.; Kapteyn, H. C.; Nardi, D. A New Regime of Nanoscale Thermal Transport: Collective Diffusion Increase Dissipation Efficiency. *Proc. Natl. Acad. Sci. U.S.A.* **2015**, *112*, 4846.

(6) Hussein, M. I.; Tsai, C.-N.; Honarvar, H. Thermal Conductivity Reduction in a Nanophononic Metamaterial versus a Nanophononic Crystal: A Review and Comparative Analysis. *Adv. Funct. Mater.* **2020**, *30*, 1906718.

(7) Hoogeboom-Pot, K. M.; Turgut, E.; Hernandez-Charpak, J. N.; Shaw, J. M.; Kapteyn, H. C.; Murnane, M. M.; Nardi, D. Nondestructive Measurement of the Evolution of Layer-Specific Mechanical Properties in sub-10 nm Bilayers Films. *Nano Lett.* **2016**, *16*, 4773.

(8) Maldovan, M. Sound and Heat Revolutions in Phononics. *Nature* **2013**, *503*, 209.

(9) Still, T.; Cheng, W.; Retsch, M.; Jonas, U.; Fytas, G. Colloidal Systems: a Promising Material Class for Tailoring Sound Propagation at High Frequencies. *J. Phys.: Condens. Matter* **2008**, *20*, 404203.

(10) Yang, L.; Yang, N.; Li, B. Extreme Low Thermal Conductivity in Nanoscale 3D Si Phononic Crystal with Spherical Pores. *Nano Lett.* **2014**, *14*, 1734.

(11) Barako, M. T.; Sood, A.; Zhang, C.; Wang, J.; Kodama, T.; Asheghi, M.; Zheng, X.; Braun, P. V.; Goodson, K. E. Quasi-Ballistic Electronic Thermal Conduction in Metal Inverse Opals. *Nano Lett.* **2016**, *16*, 2754.

(12) Chen, W.; Talreja, D.; Eichfeld, D.; Mahale, P.; Nova, N. N.; Cheng, H. Y.; Russell, J. L.; Yu, S.-Y.; Poilvert, N.; Mahan, G.; Mohney, S. E.; Crespi, V. H.; Mallouk, T. E.; Badding, J. V.; Foley, B.; Gopalan, V.; Dabo, I. Achieving Minimal Heat Conductivity by Ballistic Confinement in Phononic Metalattices. *ACS Nano* **2020**, *14*, 4235.

(13) Pikul, J. H.; Özerinç, S.; Liu, B.; Zhang, R.; Braun, P. V.; Deshpande, V. S.; King, W. P. High Strength Metallic Wood from Nanostructured Nickel Inverse Opal Materials. *Sci. Rep.* **2019**, *9*, 719.

(14) Navarro-Urrios, D.; Capuj, N. E.; Gomis-Bresco, J.; Alzina, F.; Pitanti, A.; Griol, A.; Martínez, A.; Sotomayor Torres, C. M. A Self-Stabilized Coherent Phonon Source Driven by Optical Forces. *Sci. Rep.* **2015**, *5*, 15733.

(15) Liu, Y.; Kempinger, S.; He, R.; Day, T. D.; Moradifar, P.; Yu, S.-Y.; Russell, J. L.; Torres, V. M.; Xu, P.; Mallouk, T. E.; Mohney, S. E.; Alem, N.; Samarth, N.; Badding, J. V. Confined Chemical Fluid Deposition of Ferromagnetic Metalattices. *Nano Lett.* **2018**, *18*, 546.

(16) Rana, A.; Liao, C.-T.; Iacocca, E.; Zou, J.; Pham, M.; Cating-Subramanian, E. M.; Lo, Y. H.; Ryan, S. A.; Lu, X.; Bevis, C. S.; Karl, R. M., Jr.; Glaid, A. J.; Yu, Y.-S.; Mahale, P.; Shapiro, D. A.; Yazdi, S.; Mallouk, T. E.; Osher, S. J.; Kapteyn, H. C.; Crespi, V. H.; Badding, J. V.; Tserkovnyak, Y.; Murnane, M. M.; Miao, J. Direct Observation of 3D Topological Spin Textures and their Interactions using Soft X-Ray Vector Ptychography. **2021**, arXiv:2104.12933.

(17) Yu, J.-K.; Mitrovic, S.; Tham, D.; Varghese, J.; Heath, J. R. Reduction of Thermal Conductivity in Phononic Nanomesh Structures. *Nat. Nanotechnol.* **2010**, *5*, 718.

(18) Gelbstein, Y.; Gotesman, G.; Lishzinker, Y.; Dashevsky, Z.; Dariel, M. P. Mechanical Properties of PbTe-Based Thermoelectric Semiconductors. *Scr. Mater.* **2008**, *58*, 251.

(19) Liu, W.; Jie, Q.; Kim, H. S.; Ren, Z. Current Progress and Future Challenges in Thermoelectric Power Generation: From Materials to Devices. *Acta Mater.* **2015**, *87*, 357.

(20) Jiang, J.; Chen, L.; Bai, S.; Yao, Q.; Wang, Q. Thermoelectric Properties of Textured p-Type $(Bi,Sb)_2Te_3$ Fabricated by Spark Plasma Sintering. *Scr. Mater.* **2005**, *52*, 347.

(21) Ren, F.; Wang, H.; Menchhofer, P. A.; Kiggans, J. O. Thermoelectric and Mechanical Properties of Multi-Walled Carbon Nanotube Doped $Bi_{0.4}Sb_{1.6}Te_3$ Thermoelectric Material. *Appl. Phys. Lett.* **2013**, *103*, 221907.

(22) Abad, B.; Knobloch, J. L.; Frazer, T. D.; Hernández-Charpak, J. N.; Cheng, H. Y.; Grede, A. J.; Giebink, N. C.; Mallouk, T. E.; Mahale, P.; Nova, N. N.; Tomaschke, A. A.; Ferguson, V. L.; Crespi, V. H.; Gopalan, V.; Kapteyn, H. C.; Badding, J. V.; Murnane, M. M. Nondestructive Measurements of the Mechanical and Structural Properties of Nanostructured Metalattices. *Nano Lett.* **2020**, *20*, 3306.

(23) Sanchez, C.; Boissière, C.; Grosso, D.; Laberty, C.; Nicole, L. Design, Synthesis, and Properties of Inorganic and Hybrid Thin Films Having Periodically Organized Nanoporosity. *Chem. Mater.* **2008**, *20*, 682.

(24) Taylor, D. J.; Fleig, P. F.; Hietala, S. L. Technique for Characterization of Thin Film Porosity. *Thin Solid Films* **1998**, *332*, 257.

(25) Hwang, Y. K.; Patil, K. R.; Jhung, S. H.; Chang, J.-S.; Ko, Y. J.; Park, S.-E. Control of Pore Size and Condensation Rate of Cubic Mesoporous Silica Thin Films Using a Swelling Agent. *Microporous Mesoporous Mater.* **2005**, *78*, 245.

(26) Ortel, E.; Hertwig, A.; Berger, D.; Esposito, P.; Rossi, A. M.; Kraehnert, R.; Hodoroaba, V.-D. New Approach on Quantification of Porosity of Thin Films via Electron-Excited X-Ray Spectra. *Anal. Chem.* **2016**, *88*, 7083.

(27) Dourdain, S.; Mehdi, A.; Bardeau, J. F.; Gibaud, A. Determination of Porosity of Mesoporous Silica Thin Films by Quantitative X-Ray Reflectivity Analysis and GISAXS. *Thin Solid Films* **2006**, *495*, 205.

(28) Thommes, M.; Kaneko, K.; Neimark, A.; Olivier, J.; Rodriguez-Reinoso, F.; Rouquerol, J.; Sing, K. Physisorption of Gases, with Special Reference to the Evaluation of Surface Area and Pore Size Distribution (IUPAC Technical Report). *Pure Appl. Chem.* **2015**, *87*, 1051.

(29) Baklanov, M. R.; Mogilnikov, K. P.; Polovinkin, V. G.; Dultsev, F. N. Determination of Pore Size Distribution in Thin Films by Ellipsometric Porosimetry. *J. Vac. Sci. Technol., B: Microelectron. Nanometer Struct.–Process., Meas., Phenom.* **2000**, *18*, 1385.
(30) Petkov, M. P.; Wang, C. L.; Weber, M. H.; Lynn, K. G.; Rodbell, K. P. Positron Annihilation Techniques Suited for Porosity Characterization of Thin Films. *J. Phys. Chem. B* **2003**, *107*, 2725.
(31) Galy, T.; Marszewski, M.; King, S.; Yan, Y.; Tolbert, S. H.; Pilon, L. Comparing Methods for Measuring Thickness, Refractive Index, and Porosity of Mesoporous Thin Films. *Microporous Mesoporous Mater.* **2020**, *291*, 109677.
(32) Kuai, S.-L.; Hu, X.-F.; Haché, A.; Truong, V.-V. High-quality Colloidal Photonic Crystals Obtained by Optimizing Growth Parameters in a Vertical Deposition Technique. *J. Cryst. Growth* **2004**, *267*, 317.
(33) Russell, J. L.; Noel, G. H.; Warren, J. M.; Tran, N.-L.; Mallouk, T. E. Binary Colloidal Crystal Films Grown by Vertical Evaporation of Silica Nanoparticle Suspensions. *Langmuir* **2017**, *33*, 10366.
(34) Pryor, A., Jr.; Yang, Y.; Rana, A.; Gallagher-Jones, M.; Zhou, J.; Lo, Y. H.; Melinte, G.; Chiu, W.; Rodriguez, J. A.; Maio, J. GENFIRE: A Generalized Fourier Iterative Reconstruction Algorithm for High-Resolution 3D Imaging. *Sci. Rep.* **2017**, *7*, 10409.
(35) van Heel, M.; Schatz, M. Fourier Shell Correlation Threshold Criteria. *J. Struct. Biol.* **2005**, *151*, 250.
(36) Turoňová, B.; Marsalek, L.; Slusallek, P. On Geometric Artifacts in Cryo Electron Tomography. *Ultramicroscopy* **2016**, *163*, 48.
(37) Perona, P.; Malik, J. Scale-Space and Edge Detection Using Anisotropic Diffusion. *IEEE Trans. Pattern Anal. Mach. Intell.* **1990**, *12*, 629.
(38) Sheppard, A. P.; Sok, R. M.; Averdunk, H. Techniques for Image Enhancement and Segmentation of Tomographic Images of Porous Materials. *Phys. A* **2004**, *339*, 145.
(39) *MATLAB 2019b*; copyright of The Mathworks, Inc, 2019.
(40) Otsu, N. A Threshold Selection Method from Gray-Level Histograms. *IEEE Trans. Syst. Man Cybern.* **1979**, *9*, 62.
(41) Bradley, D.; Roth, G. Adaptive Thresholding Using the Integral Image. *J. Graph. Tools* **2007**, *12*, 13.
(42) Arthur, D.; Vassilvitskii, S. K-means++: The Advantages of Careful Seeding. *SODA '07: Proceedings of the Eighteenth Annual ACM-SIAM Symposium on Discrete Algorithms*, New Orleans, LA, January 2007; pp 1027−1035.
(43) Iassonov, P.; Gebrenegus, T.; Tuller, M. Segmentation of X-Ray Computed Tomography Images of Porous Materials: A Crucial Step for Characterization and Quantitative Analysis of Pore Structures. *Water Resour. Res.* **2009**, *45*, W09415.
(44) Meyer, F. Topographic Distance and Watershed Lines. *Signal Process.* **1994**, *38*, 113.
(45) Hernandez-Charpak, J. N.; Hoogeboom-Pot, K. M.; Li, Q.; Frazer, T. D.; Knobloch, J. L.; Tripp, M.; King, S. W.; Anderson, E. H.; Chao, W.; Murnane, M. M.; Kapteyn, H. C.; Nardi, D. Full Characterization of the Mechanical Properties of 11-50 nm Ultrathin Films: Influence of Network Connectivity on the Poisson's Ratio. *Nano Lett.* **2017**, *17*, 2178.
(46) Thomsen, C.; Grahn, H. T.; Maris, H. J.; Tauc, J. Surface Generation and Detection of Phonons by Picosecond Light Pulses. *Phys. Rev. B: Condens. Matter Mater. Phys.* **1986**, *34*, 4129.
(47) Matsuda, O.; Larciprete, M. C.; Li Voti, R.; Wright, O. B. Fundamentals of Picosecond Laser Ultrasonics. *Ultrasonics* **2015**, *56*, 3.
(48) Auld, B. A. *Acoustic Fields and Waves in Solids*; Wiley: New York, 1973; Vol. 2.
(49) Rundquist, A.; Durfee, C. G., III; Chang, Z.; Herne, C.; Backus, S.; Murnane, M. M.; Kapteyn, H. C. Phase-Matched Generation of Coherent Soft X-Rays. *Science* **1998**, *280*, 1412.
(50) Tobey, R. I.; Siemens, M. E.; Cohen, O.; Murnane, M. M.; Kapteyn, H. C.; Nelson, K. A. Ultrafast Extreme Ultraviolet Holography: Dynamic Monitoring of Surface Deformation. *Opt. Lett.* **2007**, *32*, 286.
(51) Li, Q.; Hoogeboom-Pot, K.; Nardi, D.; Murnane, M. M.; Kapteyn, H. C.; Siemens, M. E.; Anderson, E. H.; Hellwig, O.; Dobisz, E.; Gurney, B.; Yang, R.; Nelson, K. A. Generation and Control of Ultrashort-Wavelength Two-Dimensional Surface Acoustic Waves at Nanoscale Interfaces. *Phys. Rev. B: Condens. Matter Mater. Phys.* **2012**, *85*, 195431.
(52) Frazer, T. D.; Knobloch, J. L.; Hoogeboom-Pot, K. M.; Nardi, D.; Chao, W.; Falcone, R. W.; Murnane, M. M.; Kapteyn, H. C.; Hernández-Charpak, J. N. Engineering Nanoscale Thermal Transport: Size- and Spacing-Dependent Cooling of Nanostructures. *Phys. Rev. Appl.* **2019**, *11*, 024042.
(53) Nardi, D.; Banfi, F.; Giannetti, C.; Revaz, B.; Ferrini, G.; Parmigiani, F. Pseudosurface Acoustic Waves in Hypersonic Surface Phononic Crystals. *Phys. Rev. B: Condens. Matter Mater. Phys.* **2009**, *80*, 104119.
(54) Nardi, D.; Travagliati, M.; Siemens, M. E.; Li, Q.; Murnane, M. M.; Kapteyn, H. C.; Ferrini, G.; Parmigiani, F.; Banfi, F. Probing Thermomechanics at the Nanoscale: Impulsively Excited Pseudosurface Acoustic Waves in Hypersonic Phononic Crystals. *Nano Lett.* **2011**, *11*, 4126.
(55) do Rosário, J. J.; Berger, J. B.; Lilleodden, E. T.; McMeeking, R. M.; Schneider, G. A. The Stiffness and Strength of Metamaterials Based on the Inverse Opal Architecture. *Extreme Mech. Lett.* **2017**, *12*, 86.
(56) *COMSOL Multiphysics v. 5.3a*; COMSOL AB: Stockholm, Sweden, 2018. www.comsol.com.
(57) Hopcroft, M. A.; Nix, W. D.; Kenny, T. W. What is the Young's Modulus of Silicon? *J. Microelectromech. Syst.* **2010**, *19*, 229.
(58) Sharpe, W. N.; Hemker, K. J.; Edwards, R. L. Mechanical Properties of MEMS Materials. *AFRL-IF-RS-TR-2004-76 Final Technical Report*, March 2004.
(59) Lide, D. R. *CRC Handbook of Chemistry and Physics*, 85th ed.; CRC Press: New York, 2005.
(60) Bellet, D.; Lamagnère, P.; Vincent, A.; Bréchet, Y. Nanoindentation Investigation of the Young's Modulus of Porous Silicon. *J. Appl. Phys.* **1996**, *80*, 3772.
(61) Martini, R.; Depauw, V.; Gonzalez, M.; Vanstreels, K.; Nieuwenhuysen, K.; Gordon, I.; Poortmans, J. Mechanical Properties of Sintered Meso-Porous Silicon: a Numerical Model. *Nanoscale Res. Lett.* **2012**, *7*, 597.
(62) Ogi, H.; Masuda, S.; Nagakubo, A.; Nakamura, N.; Hirao, M.; Kondou, K.; Ono, T. Impact of Interface Stiffness in Surface-Wave Resonances on Nanostrip-Attached Substrates. *Phys. Rev. B* **2016**, *93*, 024112.
(63) Al-Bayati, A. H.; Orrman-Rossiter, K. G.; van den Berg, J. A.; Armour, D. G. Composition and Structure of the Native Si Oxide by High Depth Resolution Medium Energy Ion Scattering. *Surf. Sci.* **1991**, *241*, 91.
(64) Bansal, N. P.; Doremus, R. H. *Handbook of Glass Properties*; Academic Press, Inc.: New York, 1986.
(65) Fakiri, S.; Montagne, A.; Rahmoun, K.; Iost, A.; Ziouche, K. Mechanical Properties of Porous Silicon and Oxidized Porous Silicon by Nanoindentation Technique. *Mater. Sci. Eng., A* **2018**, *711*, 470.
(66) www.tomviz.org, 2021.
(67) Peli, S.; Cavaliere, E.; Benetti, G.; Gandolfi, M.; Chiodi, M.; Cancellieri, C.; Giannetti, C.; Ferrini, G.; Gavioli, L.; Banfi, F. Mechanical Properties of Ag Nanoparticle Thin Films Synthesized by Supersonic Cluster Beam Deposition. *J. Phys. Chem. C* **2016**, *120*, 4673.
(68) Benetti, G.; Caddeo, C.; Melis, C.; Ferrini, G.; Giannetti, C.; Winckelmans, N.; Bals, S.; Van Bael, M. J.; Cavaliere, E.; Gavioli, L.; Banfi, F. Bottom-Up Mechanical Nanometrology of Granular Ag Nanoparticles Thin Films. *J. Phys. Chem. C* **2017**, *121*, 22434.

https://doi.org/10.1021/acsami.2c09360
ACS Appl. Mater. Interfaces 2022, 14, 41316−41327